



High Bragg reflectivity of diamond crystals exposed to multi-kW mm⁻² X-ray beams

Tomasz Kolodziej,^{a*‡} Yuri Shvyd'ko,^{a*} Deming Shu,^a Steven Kearney,^a Stanislav Stoupin,^b Wenjun Liu,^a Thomas Gog,^{a,c} Donald A. Walko,^a Jin Wang,^a Ayman Said,^a Tim Roberts,^a Kurt Goetze,^a Maria Baldini,^d Wenge Yang,^d Timothy Fister,^e Vladimir Blank,^f Sergey Terentyev^f and Kwang-Je Kim^a

Received 21 December 2017

Accepted 23 May 2018

Edited by M. Yabashi, RIKEN SPring-8 Center, Japan

‡ Now at AGH University of Science and Technology, Academic Centre for Materials and Nanotechnology, A. Mickiewicza 30 Avenue, Krakow 30-059, Poland.

Keywords: diamond; X-ray optics; radiation damage; X-ray free-electron laser oscillators; Bragg reflectivity.

^aAdvanced Photon Source, Argonne National Laboratory, Lemont, IL 60439, USA, ^bCornell High Energy Synchrotron Source, Cornell University, Ithaca, NY 14853, USA, ^cDynamic Compression Sector, Institute of Shock Physics, Washington State University, Lemont, IL 60439, USA, ^dHigh Pressure Synergetic Consortium, Advanced Photon Source, Lemont, IL 60439, USA, ^eChemical Sciences and Engineering Division, Argonne National Laboratory, Lemont, IL 60439, USA, and ^fTechnological Institute for Superhard and Novel Carbon Materials, 142190 Troitsk, Russian Federation. *Correspondence e-mail: tomasz.kolodziej@agh.edu.pl, shvydko@aps.anl.gov

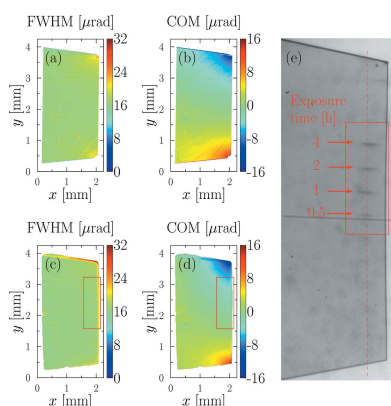
X-ray free-electron lasers in the oscillator configuration (XFEL) are future fully coherent hard X-rays sources with ultrahigh spectral purity. X-ray beams circulate in an XFEL optical cavity comprising diamond single crystals. They function as high-reflectance (close to 100%), narrowband (~ 10 meV) Bragg backscattering mirrors. The average power density of the X-ray beams in the XFEL cavity is predicted to be as high as ~ 10 kW mm⁻². Therefore, XFEL feasibility relies on the ability of diamond crystals to withstand such a high radiation load and preserve their high reflectivity. Here the endurance of diamond crystals to irradiation with multi-kW mm⁻² power density X-ray beams is studied. It is shown that the high Bragg reflectivity of the diamond crystals is preserved after the irradiation, provided it is performed at $\sim 1 \times 10^{-8}$ Torr high-vacuum conditions. Irradiation under 4×10^{-6} Torr results in a ~ 1 meV shift of the Bragg peak, which corresponds to a relative lattice distortion of 4×10^{-8} , while the high Bragg reflectivity stays intact.

1. Introduction

Recent advances in accelerator-based diffraction-limited storage-ring synchrotrons (Eriksson *et al.*, 2014; Hettel, 2014) and free-electron lasers (FELs) (Emma *et al.*, 2010; Ishikawa *et al.*, 2012) address longstanding aspirations for hard X-ray sources with ultimate brilliance, coherence and narrow spectral bandwidth.

X-ray free-electron laser oscillators (XFELs) (Kim *et al.*, 2008; Kim & Shvyd'ko, 2009) are one possible realization of FELs. They promise to generate radiation of unprecedented spectral purity, coherence and average brightness in a hard X-ray regime. In this low-gain XFEL device, X-rays generated by electrons in an undulator circulate in a low-loss optical cavity built from Bragg-reflecting crystals with close to 100% reflectivity and a ~ 10 meV bandwidth. Due to the unique combination of high transparency to X-rays, excellent thermal conductivity (Prelas *et al.*, 1998), low thermal expansion (Stoupin & Shvyd'ko, 2010, 2011) and, most importantly, close to 100% reflectivity in Bragg diffraction (Shvyd'ko *et al.*, 2010, 2011), only diamond exhibits the required set of attributes for Bragg reflecting mirrors in the XFEL cavity.

The high crystal reflectivity in Bragg diffraction is only possible if the crystal structure is perfect within several X-ray extinction lengths (Shvyd'ko, 2004; Stoupin & Shvyd'ko,



2011). For the required narrowband $\sim 1\text{--}10$ meV Bragg reflections (Lindberg *et al.*, 2011), the extinction lengths are in the $100\ \mu\text{m}$ to $10\ \mu\text{m}$ range in the hard X-ray regime. This means that, for the diamond crystals to perform as high-reflectance mirrors, their crystal structure should be perfect in a large volume comprising about 10^7 periodically arranged atomic reflecting planes.

In the current design, the power density of X-ray beams in the XFEL cavity is predicted to be up to $\sim 10\ \text{kW mm}^{-2}$ (Kim *et al.*, 2018). Such a beam would melt steel within a fraction of a millisecond. Although diamond crystals are known for their high radiation hardness (Prelas *et al.*, 1998), it is an open question whether they would survive and, most importantly, maintain their high Bragg reflectivity during continuous exposure to X-ray beams with such a high power density.

Radiation resilience of diamond crystals has been studied before (Als-Nielsen *et al.*, 1994). However, these studies were not as precise as we require. To verify that the crystal perfection is preserved in such large volumes, crystal reflectivity using narrow-band (meV) reflections with large extinction lengths must be measured with monochromatic X-rays with an even narrower bandwidth.

In the present paper, we report on reflectivity measurements of $23.77\ \text{keV}$ X-rays with a $1\ \text{meV}$ bandwidth in Bragg backreflection from a $100\ \mu\text{m}$ -thick diamond crystal, which was previously homogeneously irradiated through the crystal thickness with $8\ \text{keV}$ X-ray beams with a power density of up to $12.5\ \text{kW mm}^{-2}$. The Bragg reflection features a $6\ \text{meV}$ bandwidth and $100\ \mu\text{m}$ extinction length.

2. Methods

2.1. Focusing pink undulator beams to $\sim 12\ \text{kW mm}^{-2}$ power density

Undulators at state-of-the-art high-energy X-ray synchrotron radiation facilities generate photon beams with an average power of $\gtrsim 100\ \text{W}$, $\sim 1\ \text{mm} \times 1\ \text{mm}$ in cross section, and with about $200\ \text{eV}$ bandwidth in the first harmonic. The time-averaged power density of $\sim 10\ \text{kW mm}^{-2}$ required for our diamond irradiation experiments can only be achieved by focusing such a pink undulator X-ray beam to a small spot of $\sim 20\text{--}50\ \mu\text{m}$.

It is difficult to irradiate crystals with the high-power pink micro-focused undulator beam and to probe the crystal

reflectivity *in situ* with X-rays of meV-bandwidth and with micrometre spatial resolution. This would require two independent X-ray sources, or the use of an X-ray beam-splitter system. We performed irradiation and reflectivity measurements sequentially at different beamlines at the Advanced Photon Source (APS) synchrotron radiation facility for the present work.

We used pink-beam focusing capabilities that already exist at the APS. In initial experiments, X-rays were focused with Kirkpatrick–Baez mirrors to $\sim 4\ \text{kW mm}^{-2}$ at the 34-ID-E beamline (Liu *et al.*, 2005) and to $\sim 9\ \text{kW mm}^{-2}$ at the 35-ID-B beamline at the Dynamic Compression Sector (Capatina *et al.*, 2016). Eventually, we designed a dedicated pink-beam focusing system for use in final decisive experiments at beamline 7-ID (Walko *et al.*, 2016).

A schematic of the experimental setup at 7-ID is shown in Fig. 1. The $8\ \text{keV}$ photons of the first undulator harmonic were focused by in-vacuum water-cooled beryllium parabolic compound refractive lenses (CRLs) (Snigirev *et al.*, 1996; Lengeler *et al.*, 1999).

The power density of the focused pink beam was measured indirectly by scattering the beam, after it passed through the irradiated diamond crystal, from a $10\ \mu\text{m}$ Al foil to a Si PIN diode (D) (see Fig. 1). The Al foil and the PIN diode were calibrated earlier in a separate experiment using a monochromatic beam of known flux.

The measured power was $12.5\ \text{W}$. The beam size was $50\ \mu\text{m}$ (H) \times $20\ \mu\text{m}$ (V) (full width at half-maximum, FWHM) as measured by the knife-edge scans of the focal spot with sharp edges of the irradiated diamond crystal. The resulting power density was $\sim 12.5\ \text{kW mm}^{-2}$. We increased the irradiated area in the experiment to $50\ \mu\text{m}$ (H) \times $50\ \mu\text{m}$ (V) by rastering the crystal vertically.

2.2. Bragg reflectivity of meV X-ray beams with micrometre resolution

Because the irradiation spot size is small, methods must be developed to probe the crystal Bragg reflectivity with micrometre spatial resolution. Microfocused X-ray beams cannot be used, because they have angular spreads much larger than Bragg reflection widths. Instead, we can apply X-ray Bragg diffraction sequential topography techniques, which use position-sensitive detectors with micrometre spatial resolution (Lübbert *et al.*, 2000). In this approach, Bragg reflection dependences are recorded as a function of the angle of inci-

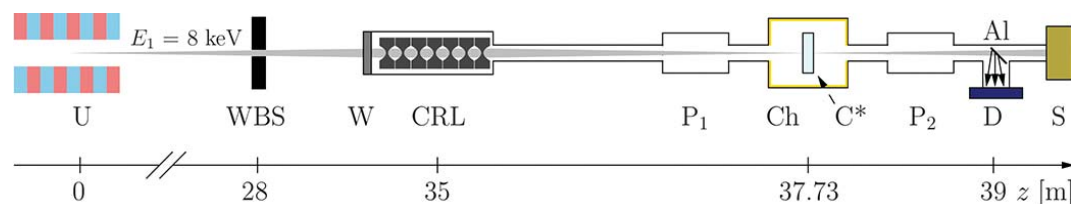


Figure 1

Scheme of the irradiation experiment at the APS undulator beamline 7-ID. Diamond crystal C^* is exposed to a $12.5\ \text{kW mm}^{-2}$ power density beam in a vacuum chamber (Ch). Other components are: U, undulator; WBS, white-beam slits; W, entrance beryllium window; CRL, compound refractive lens; P_1 , P_2 , ion pumps; Al, scattering $10\ \mu\text{m}$ Al foil; D, Si PIN diode as a flux monitor; S, beam stop.

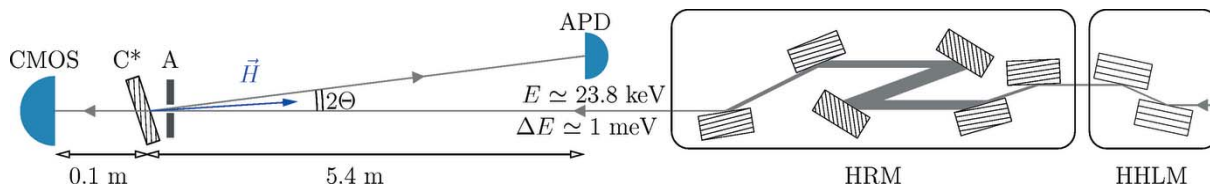


Figure 2

Experimental schemes for measuring Bragg reflectivity (with APD) and Bragg diffraction topography maps in transmission (with CMOS) of irradiated diamond single crystal C* using 23.8 keV X-rays with a $\Delta E \approx 1$ meV bandwidth, at the APS beamline 30-ID. HHLM = high-heat-load monochromator (1 eV bandwidth); HRM = high-resolution monochromator (1 meV bandwidth); C* = diamond single crystal set into the (13 3 3) Bragg backreflection with a scattering angle $\pi - 2\Theta$ ($\Theta = 1$ mrad); APD = avalanche photodiode; A = circular (30 μm -diameter) aperture used for the reflectivity measurements with the APD; CMOS = two-dimensional detector used for the topography measurements. See text for more details.

dence or photon energy by detector pixels, each looking at a certain crystal spot. A dedicated computer code (Stoupin, 2015) evaluates reflection dependences for each pixel and calculates crystal Bragg reflection maps, such as the crystal peak reflectivity map, FWHM map and reflection peak position map (*i.e.* centre-of-mass, COM position).

We know from previous studies (Shvyd'ko *et al.*, 2010, 2011) that Bragg reflectivity of the highest-quality synthetic diamond crystals is very high, almost matching theoretical limits (close to 100%), provided the crystal thickness is much larger than the extinction length. Absolute reflectivity is not easy to measure, especially if high spatial selectivity is required. However, these measurements are not required if the topography approach is used. Indeed, the reflectivity values measured in the irradiated areas can be directly compared with the reflectivity in non-irradiated areas measured in the same experiment, which provides information on whether the irradiation produced any detrimental effect on Bragg reflectivity and therefore on crystal structure.

Sequential topography is well developed for low-indexed Bragg reflections at small Bragg angles θ (Stoupin *et al.*, 2016). The method's sensitivity to crystal lattice deformations as derived from Bragg's law is $\delta d/d = \delta\theta/\tan\theta$, where $\delta\theta$ is either a variation of the COM or of the FWHM. Angular variations of a few microradians can be easily measured. Therefore, the method sensitivity is $\delta d/d \lesssim 10^{-6}$ for the low-indexed (004) Bragg reflection in diamond ($\theta = 58^\circ$ at $E = 8.2$ keV) used in this study.

However, this technique cannot be directly applied to reflectivity measurements with high-indexed Bragg reflections in backscattering. Note that backscattering geometry is essential for accurate reflectivity measurements, because it is minimally sensitive to the angular spread of the incident X-rays. Furthermore, high-indexed reflections with large extinction lengths are required to probe the whole depth of the crystal. Backscattering geometry measures the energy dependences of Bragg reflectivity (instead of the angular dependences), with the energy of the highly monochromatic photons with a 1 meV bandwidth varied by the high-resolution monochromator (HRM) (Toellner *et al.*, 2011) (see Fig. 2).

Backscattering geometry with the reflected beam at a small angle 2Θ ($\Theta \approx 1$ mrad) to the incident beam axis requires the X-ray detector to be placed at a large distance from the sample ($L \approx 5$ m in our case; see Fig. 2) to clear the path for the

incident beam. Although the divergence of the incident beam was relatively small, $\Delta\theta \approx 10$ μrad , the image of a point on the sample would be significantly blurred by $L\Delta\theta \approx 50$ μm .

The problem can be solved by taking advantage of the high X-ray transparency of diamond and measuring complementary Bragg diffraction dependences in transmission. The diamond crystal reaches simultaneously the minimum transmissivity and the maximum Bragg reflectivity, while scanning the incoming photon energy with the HRM. The transmission dependences feature the same Bragg reflection width, position and depth equal to the absolute Bragg reflectivity. The two-dimensional X-ray pixel detector was installed directly behind the crystal (see Fig. 2). The ANDOR Neo sCMOS camera used in the experiment as the two-dimensional detector was equipped with magnifying optics and scintillators and had an overall 0.65 $\mu\text{m} \times 0.65$ μm pixel resolution, which defined ultimate spatial resolution of the method. For further details, see Stoupin *et al.* (2018).

The method's sensitivity to crystal lattice deformations in the extreme backscattering case ($\theta \rightarrow 90^\circ$) is $\delta d/d = \delta E/E$, where δE is an energy variation of the Bragg reflection peak (transmission's minimum) position or its width. In particular, it is $\delta d/d \approx 10^{-8}$ for the high-order (13 3 3) Bragg reflection used in our reflectivity studies with 23.77 keV X-rays with a 1 meV bandwidth, because in this case $\delta E \approx 0.1$ meV could be resolved.

The transmission topography technique was developed over the course of our studies. In the first experiments, however, we used instead a small pinhole A with an opening of 30 μm^1 in front of and very close to the crystal (see Fig. 2), for spatially selective reflectivity measurements across the irradiated crystal.

2.3. Diamond crystals

The highest-quality nearly flawless diamond single crystals were used in these studies. The crystals were grown at the Technological Institute for Superhard and Novel Carbon Materials (Troitsk, Russia) by a temperature gradient method under high pressure and high temperature (HPHT) [see Shvyd'ko *et al.* (2017) for a review and references]. The crystal

¹ The pinhole in a Pt foil was laser drilled with the apparatus of the HPCAT group at the APS (Hrubiak *et al.*, 2015).

thickness was chosen to be $\sim 100\ \mu\text{m}$: first, this was much thinner than a $\sim 650\ \mu\text{m}$ photo-absorption length of the 8 keV photons used for irradiation, to ensure homogeneous irradiation through the whole crystal, and, second, it was chosen to be close to the $100\ \mu\text{m}$ extinction length of the high-order (13 3 3) Bragg reflection used for the reflectivity studies in backscattering. In this case, the whole depth of the irradiated crystal could be probed in the reflectivity studies.

Figs. 3(a) and 3(b) show the FWHM and COM Bragg reflectivity maps, respectively, measured on the selected crystal before irradiation using the sequential topography setup (Stoupin *et al.*, 2016) at the APS beamline 1-BM (Macrander *et al.*, 2016). We used the previously mentioned (004) low-indexed Bragg reflection. The FWHM maps reveal a very homogeneous crystal quality with an almost theoretical FWHM of Bragg reflections in the inspected area of $2\ \text{mm} \times 4\ \text{mm}$, which confirms a very high crystal quality. The COM maps reveal some strain in the crystal corners due to the crystal's mount. The irradiation was performed in the central area, as indicated on the crystal photograph in Fig. 3(e) by the red rectangle, featuring the smallest strain.

We conducted crystal irradiation in vacuum to avoid crystal degradation through oxidation and other chemical reactions. To reduce possible carbon deposition on the diamond crystal from the stainless steel vacuum chamber walls (Ohashi *et al.*, 2016), the inner surface of the chamber was plated with a

$50\ \mu\text{m}$ -thick gold layer. The crystal was mounted on a water-cooled copper holder in the sample chamber for effective transfer of heat resulting from X-ray photo-absorption. The crystal temperature did not exceed 22°C during irradiation. More technical details on the irradiation setup presented in Fig. 1 are given by Kearney *et al.* (2017).

3. Irradiation and reflectivity measurements

3.1. Irradiation with $9\ \text{kW}\ \text{mm}^{-2}$ X-ray beams at 4×10^{-6} Torr

In the initial irradiation experiment, we used an X-ray beam of $9\ \text{kW}\ \text{mm}^{-2}$ power density and a $130\ \mu\text{m}$ (H) \times $30\ \mu\text{m}$ (V) spot size on the diamond crystal. The sample chamber was evacuated to 4×10^{-6} Torr. The irradiation time of different crystal spots varied from 1 min to 4 h. In the areas irradiated for more than half an hour, blackening was clearly observed, as seen in the photograph of the diamond crystal (Fig. 3e) taken after the irradiation experiment.

However, no indications of any changes in crystal structure or quality could be observed in the (004) Bragg reflectivity maps. Indeed, the FWHM and COM maps measured after irradiation, see Figs. 3(c) and 3(d), are practically identical to those in Figs. 3(a) and 3(b) measured before irradiation.

However, we detected the impact of the irradiation on the crystal structure using the high-indexed (13 3 3) Bragg reflection, featuring a two-orders-of-magnitude larger sensitivity to crystal deformations (see §2.2 for details).

Fig. 4 shows the (13 3 3) Bragg peak reflectivity (a), FWHM (b) and COM (c) derived from energy dependences of the Bragg reflectivity measured across the irradiated spots. The energy dependences were measured with the APD (see Fig. 2). Fig. 4(d) shows examples of the energy dependences measured at $x = 0.05$ in the spot irradiated for 1 h (data shown in red) and in the neighbouring not-irradiated spots at $x = \pm 0.15\ \text{mm}$ (blue and violet). Solid lines are Gaussian profiles fitted to the experimental data. All reflection curves feature the same width $\Delta E = 5.8\ \text{meV}$ (FWHM) and intensity. The only difference is that the peak in the irradiated spot is shifted by $\delta E = -1.6\ \text{meV}$. The X-ray beam size and position on the crystal were defined by the $30\ \mu\text{m}$ circular pinhole A installed in front of the crystal.

Although there was only insignificant variation (less than 1%) in the intensity or width of the Bragg reflections [see Figs. 4(a) and 4(b), respectively], clear shifts of the reflection peaks were observed at the irradiated spots [see Fig. 4(c)]. Note that the strong features in all graphs at $x \simeq 1.1\ \text{mm}$ were due to an intrinsic localized crystal defect.

The shift of the Bragg reflection peak position with the reflectivity and width unchanged may occur only due to a homogeneous lattice distortion (homogeneous change of the lattice parameter d) through the whole crystal thickness. Was it an irradiation-induced change in the crystal volume due to, for example, the transition of some carbon atoms into interstitial positions? This would be a small effect, but still an effect

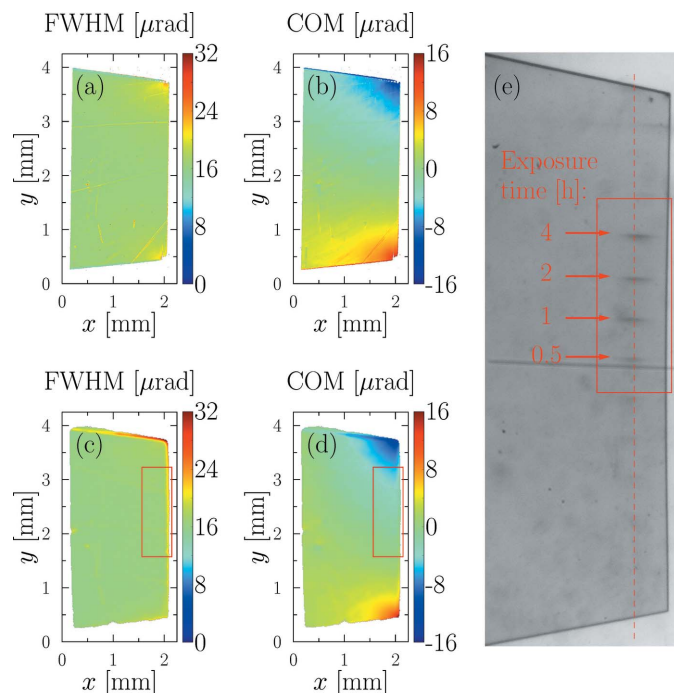


Figure 3

The (004) Bragg reflectivity maps and a photograph of the diamond single crystal irradiated with X-rays of a $9\ \text{kW}\ \text{mm}^{-2}$ power density. (a, c) FWHM maps before and after irradiation, respectively. (b, d) The relevant COM maps. (e) Photograph of the crystal with black stripes revealing the irradiated spots. The red rectangles on the maps and on the photograph indicate the location of the irradiated area. The numbers indicate the exposure time.

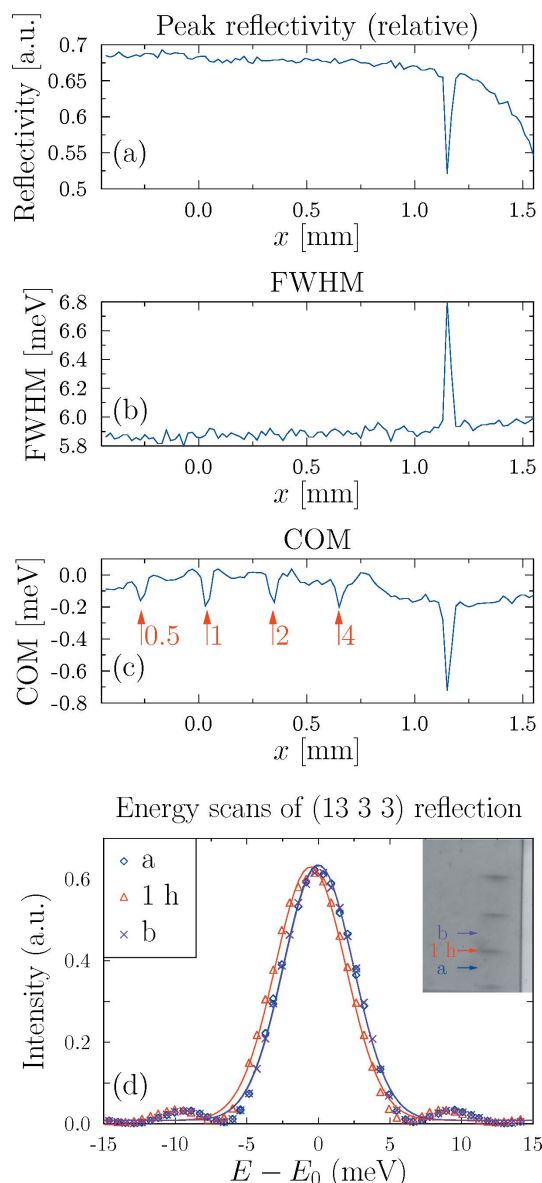


Figure 4 (a) The (13 3 3) Bragg reflectivity, (b) FWHM and (c) COM of the diamond crystal irradiated with 9 kW mm^{-2} X-rays in vacuum at 4×10^{-6} Torr. Red arrows and exposure time in (c) mark positions of the black irradiated spots visible in Fig. 3(e). The pronounced features at $x = 1.1 \text{ mm}$ are due to a crystal defect. (d) Bragg reflectivity as a function of photon energy measured at $x = 0.05$ in the spot irradiated for 1 h (data shown in red) and in the neighbouring not irradiated areas $x = \pm 0.15 \text{ mm}$ (blue and violet). Solid lines are Gaussian profiles fitted to the experimental data with the parameters provided in the text.

due to radiation damage. Or maybe the distortion and the shift were caused by something deposited on the crystal surface during the irradiation, such as the thin black film? Atomic force microscopy measurements indeed revealed a $\sim 5\text{--}10 \text{ nm}$ -thick deposition. Raman spectra taken from the spots exhibited pronounced narrow diamond-like peaks at 1332 cm^{-1} with broad weak pedestals in the $1400\text{--}1600 \text{ cm}^{-1}$ range, but no sharp modes characteristic of graphite.

The irradiation-induced thin film deposition on the crystal surface is not really radiation damage. However, can such a

thin surface film produce measurable homogeneous bulk deformation?

Additional studies were performed to understand which of the two causes – surface or bulk – resulted in the shift of the Bragg peaks.

3.2. Effect of crystal annealing

The first question to answer was whether the blackening of the irradiated spots was responsible for the observed diamond lattice distortion.

We know from our previous experience that annealing diamond in air at 650°C results in burning carbon compounds on the diamond surface while keeping the crystal bulk intact. This can even remove moderate crystal strain (Kolodziej *et al.*, 2016). We thus annealed the crystal which had been irradiated in the 9 kW mm^{-2} beam in air for 3 h. As a result, all irradiation-induced black spots disappeared along with any measurable crystal lattice distortion.

Fig. 5 presents the (13 3 3) Bragg reflection topography maps in transmission (see §2 for details) measured on the diamond crystal after annealing. We mapped the same crystal area as in Fig. 4. The red arrows with exposure times indicate the locations of the irradiated spots. There is no longer any evidence of the Bragg reflection shifts on the COM map in Fig. 5(c). Only the strong features at $x \simeq 1.1 \text{ mm}$ in Figs. 5(a)–5(c) are still present, the same as in Figs. 4(a)–4(c), due to the localized crystal defect.

The recovery of the diamond crystal lattice distortion upon annealing clearly proves that the blackening of the irradiated spots is related to the lattice distortion. However, this still does not tell us whether it is an irradiation-induced surface or bulk

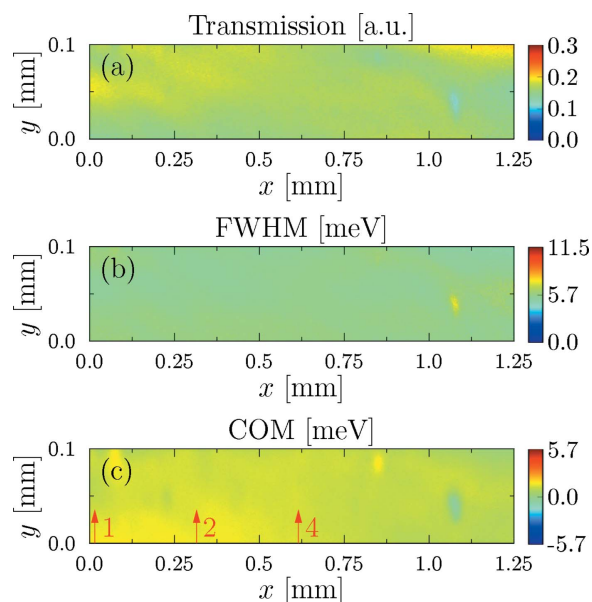
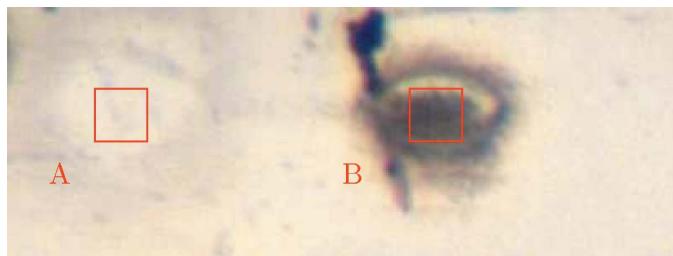


Figure 5 The (13 3 3) Bragg reflection topography maps in transmission measured after annealing the diamond crystal previously irradiated with 9 kW mm^{-2} X-rays. (a) Transmitted signal strength, (b) FWHM and (c) COM. The red arrows together with the exposure time indicate positions of the irradiated spots visible in Fig. 3(e); see also Fig. 4.


Figure 6

Photograph of a fragment of the diamond single crystal with spots A and B irradiated for 4 h by X-rays of the 12.5 kW mm^{-2} power density at different vacuum levels in the sample chamber: 1×10^{-8} Torr in area A, and 4×10^{-6} Torr in area B. See text for details.

effect. Annealing could have also healed irradiation-induced crystal bulk defects.

3.3. Irradiation with 12 kW mm^{-2} X-ray beams at 10^{-8} Torr

To address the ‘bulk or surface’ dilemma, we repeated the irradiation experiment in a vacuum improved by more than two orders of magnitude to 1×10^{-8} Torr, compared with 4×10^{-6} Torr in the initial experiment presented in §3.1. Additional care was taken to reduce carbon sources in the irradiation sample chamber (see §2.3 for details).

Fig. 6 shows a photograph of the diamond crystal taken after irradiation of two spots, labelled A and B, for 4 h each with a focused beam of 12.5 kW mm^{-2} power density. Irradiation of spot A was performed while the pressure of residual gases in the chamber was 1×10^{-8} Torr. Spot B was irradiated at a vacuum level two orders of magnitude lower, 4×10^{-6} Torr. There is a drastic difference: spot A is clean, while spot B is substantially blackened.

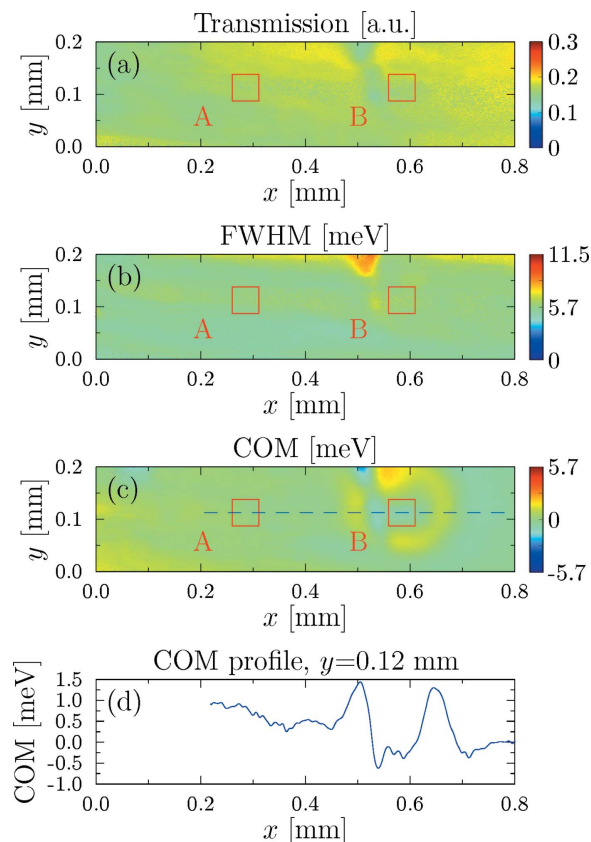
The (13 3 3) Bragg reflection topography maps measured in transmission on the diamond crystal after the irradiation are shown in Figs. 7(a)–7(c). As in the previous irradiation case [see §3.1 and Fig. 4(c)], the impact of the irradiation can be seen only on the COM map in Fig. 7(c), and even then only in the area around spot B, which was irradiated under lower vacuum conditions and blackened.

The measured COM variation around spot B is $\delta E \simeq \sim 1 \text{ meV}$ (see Fig. 7d). The corresponding relative lattice parameter variation is very small, $\delta d/d = \delta E/E = 4 \times 10^{-8}$, and undetectable by the diffraction topography of the low-indexed (0 0 4) reflection.

The results of the final experiment unambiguously show that the observed irradiation-induced crystal lattice distortion occurs due to adsorption of residual gases from the vacuum sample chamber, but only if the vacuum level in the chamber is relatively low. Apart from that, diamond crystal lattice and high-indexed Bragg reflectivity show no measurable effects from irradiation with X-rays with a $\sim 12 \text{ kW mm}^{-2}$ power density.

4. Discussion and conclusions

Very high Bragg reflectivity of X-rays from diamond crystals, close to 100% as demonstrated previously (Shvyd'ko *et al.*,


Figure 7

(a)–(c) The (13 3 3) Bragg reflection topography maps measured in transmission on the diamond crystal irradiated by X-rays of a 12.5 kW mm^{-2} power density. (d) COM of the Bragg reflection dependences along the blue dashed line in (c). Rectangles A and B indicate locations of the irradiated spots on the crystal (see Fig. 6).

2010, 2011), is critical for realization of XFEL X-ray cavities. The power density of X-rays in an XFEL cavity is expected to be very high, up to 15 kW mm^{-2} (Kim *et al.*, 2018). For XFEL feasibility, it is therefore equally critical that the high reflectivity is preserved under such harsh radiation conditions.

To verify whether this is possible, we performed irradiation experiments with undulator pink beams focused to 12 kW mm^{-2} power density on the highest-quality synthetic diamond crystal plates. We measured the reflectivity of 23.77 keV X-rays with a 1 meV bandwidth from a selected 100 μm -thick diamond crystal in the (13 3 3) Bragg back reflection, featuring a 6 meV Bragg reflection bandwidth and 100 μm extinction length.

We found that the high Bragg reflectivity, reflection width and peak position stay intact after the irradiation for 4 h, provided the irradiation was performed under $\sim 10^{-8}$ Torr high-vacuum conditions. Irradiation in a vacuum degraded to 4×10^{-6} Torr (400 times) resulted in a $\sim 1 \text{ meV}$ shift of the Bragg peak, while the high Bragg reflectivity and reflection width stayed intact. The shift was associated with a deposition on the crystal surface of a few tens of nanometres thin carbon film from residual gases, which caused a crystal deformation of $\delta d/d \simeq 4 \times 10^{-8}$ relative lattice parameter change, which was homogeneous through the crystal thickness.

We further showed that the carbon film and the crystal deformation can be completely removed by annealing the crystal in air at 650°C.

Apart from this, irradiation of the diamond crystal with the 12 kW mm⁻² power density beams resulted in no measureable impact on the Bragg reflectivity, let alone in radiation damage.

One can argue that irradiation under high-vacuum conditions but for 400 times longer [*i.e.* for 1600 h (66 days)] might generate similar crystal distortion as 4 h of irradiation under lower-vacuum conditions. We note that the adsorption effect can be mitigated by further improving vacuum in the sample chamber and by rastering the crystal in the X-ray beam.

How far are we from the radiation damage threshold? Theoretical (Medvedev *et al.*, 2013) and experimental (Gaudin *et al.*, 2013; Uhlén *et al.*, 2013) studies of diamond irradiated by femtosecond X-ray laser pulses revealed that there was a 0.7 eV per atom threshold in terms of instantaneous absorbed dose, which could lead to non-thermal graphitization of diamond. We estimate that the irradiations discussed here are about three orders of magnitude below the non-thermal graphitization threshold.

In conclusion, our results prove that diamond crystals can survive the power load within the XFEL cavity and preserve very high reflectivity. The results are equally important for high-resolution diamond crystal optics applications at high-repetition-rate XFELs generating X-rays with similar power densities (Chubar *et al.*, 2016).

Acknowledgements

We acknowledge the support of Drs Stephen Streiffer, Mark Beno, Jonathan Lang and Stephan Vogt, which enabled execution of the experiments at multiple Advanced Photon Source beamlines within a short time. We acknowledge Dr Albert Macrander and Dr Lahsen Assoufid for supporting experiments at 1-BM-B beamline of the APS. Work at the Advanced Photon Source was supported by the US Department of Energy, Office of Science, Office of Basic Energy Sciences, under Contract No. DE-AC02-06CH11357. This publication is based upon work performed at the Dynamic Compression Sector, which is operated by Washington State University under the US Department of Energy (DOE)/National Nuclear Security Administration award No. DE-NA0002442.

Funding information

Funding for this research was provided by: US Department of Energy, Office of Science, Office of Basic Energy Sciences (contract No. DE-AC02-06CH11357); US Department of Energy (DOE)/National Nuclear Security Administration (award No. DE-NA0002442).

References

Als-Nielsen, J., Freund, A., Wulff, M., Hanfland, M. & Häusermann, D. (1994). *Nucl. Instrum. Methods Phys. Res. B*, **94**, 348–350.
 Capatina, D., D’Amico, K., Nudell, J., Collins, J. & Schmidt, O. (2016). *AIP Conf. Proc.* **1741**, 030036.

Chubar, O., Geloni, G., Kocharyan, V., Madsen, A., Saldin, E., Serkez, S., Shvyd’ko, Y. & Sutter, J. (2016). *J. Synchrotron Rad.* **23**, 410–424.
 Emma, P., Akre, R., Arthur, J., Bionta, R., Bostedt, C., Bozek, J., Brachmann, A., Bucksbaum, P., Coffee, R., Decker, F.-J., Ding, Y., Dowell, D., Edstrom, S., Fisher, A., Frisch, J., Gilevich, S., Hastings, J., Hays, G., Hering, P., Huang, Z., Iverson, R., Loos, H., Messerschmidt, M., Miahnahri, A., Moeller, S., Nuhn, H.-D., Pile, G., Ratner, D., Rzepiela, J., Schultz, D., Smith, T., Stefan, P., Tompkins, H., Turner, J., Welch, J., White, W., Wu, J., Yocky, G. & Galayda, J. (2010). *Nat. Photon.* **4**, 641–647.
 Eriksson, M., van der Veen, J. F. & Quitmann, C. (2014). *J. Synchrotron Rad.* **21**, 837–842.
 Gaudin, J., Medvedev, N., Chalupský, J., Burian, T., Dastjani-Farahani, S., Hájková, V., Harmand, M., Jeschke, H. O., Juha, L., Jurek, M., Klinger, D., Krzywinski, J., Loch, R. A., Moeller, S., Nagasono, M., Ozkan, C., Saksl, K., Sinn, H., Sobierajski, R., Sovák, P., Toleikis, S., Tiedtke, K., Toufarová, M., Tschentscher, T., Vorlíček, V., Vyšín, L., Wabnitz, H. & Ziaja, B. (2013). *Phys. Rev. B*, **88**, 060101.
 Hettel, R. (2014). *J. Synchrotron Rad.* **21**, 843–855.
 Hrubciak, R., Sinogeikin, S., Rod, E. & Shen, G. (2015). *Rev. Sci. Instrum.* **86**, 072202.
 Ishikawa, T., Aoyagi, H., Asaka, T., Asano, Y., Azumi, N., Bizen, T., Ego, H., Fukami, K., Fukui, T., Furukawa, Y., Goto, S., Hanaki, H., Hara, T., Hasegawa, T., Hatsui, T., Higashiya, A., Hirono, T., Hosoda, N., Ishii, M., Inagaki, T., Inubushi, Y., Itoga, T., Joti, Y., Kago, M., Kameshima, T. & *et al.* (2012). *Nat. Photon.* **6**, 540–544.
 Kearney, S. P., Shu, D., Kolodziej, T., Kim, K.-J., Lindberg, R., Walko, D. A., Wang, J., Shvyd’ko, Yu. & Stoupin, S. (2017). *Proceedings of the 38th International Free Electron Laser Conference*, 20–25 August 2017, Santa Fe, NM, USA. MOP056.
 Kim, K.-J., Kearney, S. P., Kolodziej, T., Lindberg, R. R., Shia, X., Shu, D., Shvyd’ko, Yu., Stoupin, S., Zemella, J., Fawley, W. M., Grizzoli, W. C., Qin, W., Bane, K. L. F., Ding, Y., Emma, P. J., Hastings, J., Huang, Z., Krzywinski, J., Marcus, G., Maxwell, T. J., Blank, V. D. & Terentiev, S. (2018). *FEL2017 Conf. Proc.* To be published.
 Kim, K.-J. & Shvyd’ko, Yu. V. (2009). *Phys. Rev. ST Accel. Beams*, **12**, 030703.
 Kim, K.-J., Shvyd’ko, Yu. & Reiche, S. (2008). *Phys. Rev. Lett.* **100**, 244802.
 Kolodziej, T., Vodnala, P., Terentyev, S., Blank, V. & Shvyd’ko, Y. (2016). *J. Appl. Cryst.* **49**, 1240–1244.
 Lengeler, B., Schroer, C., Tümmler, J., Benner, B., Richwin, M., Snigireva, A., Snigireva, I. & Drakopoulos, M. (1999). *J. Synchrotron Rad.* **6**, 1153–1167.
 Lindberg, R. R., Kim, K.-J., Shvyd’ko, Yu. & Fawley, W. M. (2011). *Phys. Rev. ST Accel. Beams*, **14**, 010701.
 Liu, W., Ice, G. E., Tischler, J. Z., Khounsary, A., Liu, C., Assoufid, L. & Macrander, A. T. (2005). *Rev. Sci. Instrum.* **76**, 113701.
 Lübbert, D., Baumbach, T., Härtwig, J., Boller, E. & Pernot, E. (2000). *Nucl. Instrum. Methods Phys. Res. B*, **160**, 521–527.
 Macrander, A., Erdmann, M., Kujala, N., Stoupin, S., Marathe, S., Shi, X., Wojcik, M., Nocher, D., Conley, R., Sullivan, J., Goetze, K., Maser, J. & Assoufid, L. (2016). *AIP Conf. Proc.* **1741**, 030030.
 Medvedev, N., Jeschke, H. O. & Ziaja, B. (2013). *Phys. Rev. B*, **88**, 224304.
 Ohashi, H., Senba, Y., Yumoto, H., Koyama, T., Miura, T. & Kishimoto, H. (2016). *AIP Conf. Proc.* **1741**, 040023.
 Prelas, M. A., Popovici, G. & Bigelow, L. K. (1998). Editors. *Handbook of Industrial Diamonds and Diamond Films*. New York: Marcel Dekker, Inc.
 Shvyd’ko, Yu. (2004). *X-ray Optics – High-Energy-Resolution Applications*, Vol. 98 of *Optical Sciences*. Berlin/Heidelberg/New York: Springer.
 Shvyd’ko, Yu., Blank, V. & Terentyev, S. (2017). *MRS Bull.* **42**, 437–444.
 Shvyd’ko, Yu. V., Stoupin, S., Blank, V. & Terentyev, S. (2011). *Nat. Photon.* **5**, 539–542.

- Shvyd'ko, Yu. V., Stoupin, S., Cunsolo, A., Said, A. & Huang, X. (2010). *Nat. Phys.* **6**, 196–199.
- Snigirev, A., Kohn, V., Snigireva, I. & Lengeler, B. (1996). *Nature (London)*, **384**, 49–51.
- Stoupin, S. (2015). *Python-DTXRD*, <https://www.aps.anl.gov/Science/Scientific-Software/DTXRD>.
- Stoupin, S., Kolodziej, T., Said, A., Campello, A. & Shvyd'ko, Yu. (2018). *Proceedings of the Denver X-ray Conference (DXC 2017)*. Accepted for publication.
- Stoupin, S. & Shvyd'ko, Yu. V. (2010). *Phys. Rev. Lett.* **104**, 085901.
- Stoupin, S. & Shvyd'ko, Yu. V. (2011). *Phys. Rev. B*, **83**, 104102.
- Stoupin, S., Shvyd'ko, Yu., Trakhtenberg, E., Liu, Z., Lang, K., Huang, X., Wiczorek, M., Kasman, E., Hammonds, J., Macrander, A. & Assoufid, L. (2016). *AIP Conf. Proc.* **1741**, 050020.
- Toellner, T. S., Alatas, A. & Said, A. H. (2011). *J. Synchrotron Rad.* **18**, 605–611.
- Uhlén, F., Nilsson, D., Holmberg, A., Hertz, H. M., Schroer, C. G., Seiboth, F., Patommel, J., Meier, V., Hoppe, R., Schropp, A., Lee, H. J., Nagler, B., Galtier, E., Krzywinski, J., Sinn, H. & Vogt, U. (2013). *Opt. Express*, **21**, 8051–8061.
- Walko, D. A., Adams, B. W., Doumy, G., Dufresne, E. M., Li, Y., March, A. M., Sandy, A. R., Wang, J., Wen, H. & Zhu, Y. (2016). *AIP Conf. Proc.* **1741**, 030048.